Engineering Structures 345 (2025) 121489

Contents lists available at ScienceDirect

Engineering Structures

journal homepage: www.elsevier.com/locate/engstruct

Numerical modeling of glued laminated timber beams without finger joints: Identifying load-bearing capacity and analyzing failure mechanisms☆

Christoffer Vida *, Markus Lukacevic, Georg Hochreiner, Sebastian Pech, Josef Füssl

Institute for Mechanics of Materials and Structures, TU Wien, Karlsplatz 13/202, 1040 Vienna, Austria

ARTICLE INFO

Keywords:
Global failure criterion
Progressive damage
Laminating effect
Size effect
Glued laminated timber
XFEM

ABSTRACT

Developing simulation approaches to predict the structural behavior of glued laminated timber (GLT) beams under loading is essential for formulating efficient design concepts, particularly for large-span structures. While experimental data for GLT beams according to European standards are limited to depths of about 1 m with rather small sample sizes, a substantial knowledge gap exists for beams already used in practice with depths up to 3 m. For such large beams, conflicting size effects have been reported by simulation studies. Numerical modeling of GLT beams is challenging, e.g., the quasi-brittle nature of wood requires modeling progressive failure mechanisms and nonlinear behavior during loading. This study examines the influence of three global failure criteria on bending strength, modulus of elasticity (MOE), and damage states of simulated GLT beams without finger joints. The examination is based on data from 11 800 simulations covering seven beam sizes up to 3.3 m and two strength classes. The simulations incorporated discrete vertical and horizontal cracking and plastic deformations. The findings reveal that the choice of failure criterion significantly influences the predicted bending strength, while the MOE remains practically unchanged. A load-drop criterion most effectively captured the peak loads, highlighting the role of progressive damage accumulation. The reported damage states provide insights into the failure processes modeled in the simulations. These results underscore the importance of selecting appropriate failure criteria and mechanisms in numerical models to predict the performance of large-scale GLT beams.

1. Introduction

Wood, as a naturally growing resource, exhibits remarkable mechanical properties relative to its light weight. However, inherent characteristics of wood, such as knots, lead to greater variability in material properties compared to materials like brick or steel. The development of numerical simulation approaches has been crucial for understanding the mechanical behavior and enhancing the performance of glued laminated timber (GLT), a widely used building material.

Manufacturing GLT enables the production of beams larger than single timber boards and helps homogenize material properties, reducing variability. GLT beams are constructed by stacking and gluing laminations made from finger-jointed timber boards, allowing for laminations of virtually endless length. This manufacturing process makes GLT beams highly suitable for wide-span structures. In recent decades, beam sizes have increased, with European manufacturers now producing beams up to 3 m in depth.

The application of such large beams presents a challenge, as experimental data has mainly been gathered from smaller beams (e.g., [1–12]). Determining the change in strength with increasing structural size, known as the size effect, is practically infeasible for beams with depths up to 3 m. For smaller beams, the size effect was experimentally determined by, e.g., Aasheim and Solli [7] and Schickhofer [8]. Additionally, capturing variability in experiments requires tremendous effort when producing large sample sizes. Falk et al. [6] tested an extensive sample size of 312 beams in the same test setup, covering three strength classes.

Numerical simulation approaches offer an effective alternative to experiments, capable of modeling large-scale beams with large sample sizes. The present work focuses on GLT beams made from softwood and in compliance to European standards. Recent investigations [13–15] have utilized numerical methods to study the load-bearing capacity of homogeneous layouts according to European standards, including large-scale beams. Their results have been successfully compared to small-scale experimental data. These studies captured the varying material properties along the boards by defining weak sections, where properties such as tensile strength and modulus of elasticity (MOE)

☆ This article is part of a Special issue entitled: 'Mass Timber Systems' published in Engineering Structures.

* Corresponding author.
E-mail address: christoffer.vida@tuwien.ac.at (C. Vida).

https://doi.org/10.1016/j.engstruct.2025.121489

Available online 9 October 2025

were reduced compared to defect-free sections. Each approach used different methods to assign section-wise constant material properties [5,16–19].

A related simulation study by Lam [20] investigated the size effect in GLT beams according to North American rules. However, since factors such as the quality and grading practices influence the size effect [20], these results may not be directly comparable and are not considered further in this work.

Regarding studies based on European standards, Fink et al. [13] presented a probabilistic approach to simulate the load-bearing capacity, including an analysis of beams with depths up to 1.2 m. Frese and Blaß [14] used an updated version of the *Karlsruhe Calculation Model* [16,21,22] to investigate the size effect for beams up to 3.0 m depth. Both approaches implemented progressive failure, modeled as perfectly brittle. However, wood failure in tension is quasi-brittle, characterized by a fracture process zone ahead of the crack tip, which enables stress redistribution [23]. Modeling GLT beams with quasi-brittle fracture was addressed by Blank et al. [24]. Tapia Camú and Aicher [25] employed the extended finite element method (XFEM) with a traction–separation law to simulate quasi-brittle failure in hardwood GLT beams. For softwood GLT beams, the interaction of horizontally offset damage modeled with XFEM was addressed by implementing cohesive failure surfaces, as presented in [26]. Building on this model, the size effect for beams up to 3.3 m deep was studied in [15].

All modeling approaches accounted for progressive failure during loading, ultimately leading to global failure. However, capturing such failure mechanisms experimentally remains extremely challenging. Cracks are typically recorded after beam failure, making it difficult to identify the early damage that triggers massive crack expansion during the load drop. Moreover, visible cracks on the beam surface can differ from internal failures within the cross-section [12]. One approach that can help to localize microcracks before they are visually detected or captured by camera involves the use of acoustic emissions [27]. Acoustic emissions indicate that damage initiates at very early stages, between 5% and 20% of peak stress [28]. Moreover, microdamage occurring prior to the formation of macroscopic cracks appears to have no significant influence on global stiffness [29].

Notably, the three studies [13–15] presented varying results regarding the size effect, highlighting the significant influence of the chosen modeling approach. Each study applied a different global failure criterion to determine the beams' load-bearing capacity. The differences in failure criteria raise important questions about how these definitions affect the load-bearing capacity and the associated progressive damage states, particularly as beam sizes vary. Additionally, progressive damage states are rarely reported in the literature, leaving gaps in understanding the modeled damage mechanisms.

To analyze the influence of different global failure criteria on the load-bearing capacity and the modeled damage states across various beam sizes, we evaluated results from 11 800 simulations involving seven beam sizes and two strength classes, originally conducted in a previous study [15]. These simulations provided complete load–displacement paths, enabling us to determine load-bearing capacities using three different global failure criteria based on the mentioned studies [13–15]. Additionally, we performed a detailed analysis of the failure mechanisms implemented within the numerical approach.

In a broader context, simulation approaches like the one presented in this study can provide a valuable foundation for future data-driven models. Compared to experimental campaigns, they enable extensive sample sizes and offer insights into failure processes that are difficult to capture experimentally. These datasets can support the development of surrogate models for applications such as structural reliability analysis or the prediction of damage evolution. For example, Ni et al. [30] employed a Kriging surrogate model to predict the probability distribution of the load-bearing capacity of nonlinear structures resulting from variability in material parameters. Goswami et al. [31] used a physics-informed neural network to predict crack paths in quasi-brittle materials. These examples highlight the relevance of mechanical modeling for applications beyond conventional analysis.

This paper is organized as follows: Section 2 outlines the board properties, discusses finger joints, presents the numerical approach, details the scope of the simulation campaign, and introduces the three global failure criteria applied in this study. Section 3 examines the overall structural behavior observed during loading. Section 4 compares the strength and MOE obtained using different failure criteria, while Section 5 explores the progressive damage states related to the implemented failure mechanisms. The paper concludes with a brief summary, key conclusions, and an outlook in Section 6.

2. Materials and methods

2.1. Scope and property distinctions

This work builds on numerical simulations of GLT beam sections from a previous study [15]. First, the wooden board properties are summarized (Section 2.2), followed by a discussion on the role of finger-joint failures (Section 2.3). The modeling approach used to simulate the GLT beam sections under a constant bending moment is introduced subsequently (Section 2.4). The original simulation campaign in [15] was extensive, covering seven beam sizes and two strength classes (Section 2.5). The novelty of this work lies in evaluating the load–displacement paths using three different global failure criteria, with detailed definitions provided in Section 2.6.

It is important to differentiate between material properties and effective properties. Effective properties relate to the structural response, specifically they depend on the structure's size and loading configuration. Typically they are obtained using conventional linear elastic beam theory with homogeneous materials and assuming perfectly brittle failure. For instance, the European standard EN 14080:2013 [32] used in this work provides such effective values for bending strength and MOE of GLT beams. In contrast, material properties refer to the inherent characteristics of the material itself and are independent of the structure's size or loading configuration. The bending strength and MOE of GLT beams presented in this work represent effective properties.

2.2. Wooden board properties

The orthotropic behavior of the wooden boards was characterized by section-wise constant properties, based on the deterministic estimation procedure presented by Kandler et al. [19]. The method utilized three-dimensional reconstructions of real wooden boards using the geometric reconstruction algorithm proposed by Kandler et al. [33] that combined knot geometry and fiber course data obtained from surface laser scans during strength grading. Each board, with dimensions of 5400 mm by 90 mm by 33 mm, was divided into sections representing either defect-free wood or areas containing knots. In total, 280 reconstructed boards were used, equally distributed between strength classes T14 and T22 as per EN 338:2016 [34].

The material properties along each board were characterized by profiles of the effective longitudinal MOE E_L and the effective tensile strength f_t (Fig. 1). For the boards' stiffness, individual stiffness tensors were assigned using a micromechanical multiscale model developed by Hofstetter et al. [35]. The clear wood sections were assigned the upper bound of the MOE profile, directly corresponding to the individual unmodified stiffness tensor, while the weak sections' MOE was determined using the reconstructed sections containing knots in a finite element approach [19]. The tensile strength in weak sections was estimated using a linear regression model based on the knot area ratio [36], and a constant upper strength limit was used for clear wood sections.

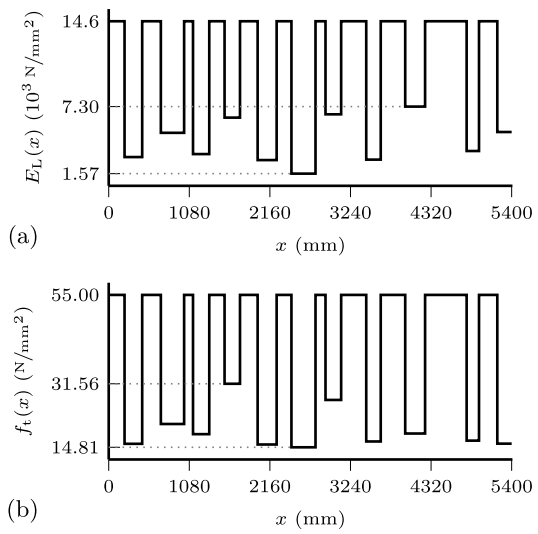

Fig. 1. Property profiles parallel to the grain, showing (a) the longitudinal MOE E_L and (b) the tensile strength f_t.

2.3. Finger joints

Finger joints enable the creation of laminations having virtually unlimited lengths from timber boards with limited length. While finger joining is necessary for manufacturing large GLT beams, the joints also introduce weak points. For example, Ehlbeck and Colling [4] identified that the bending strength of GLT beams depends primarily on two factors: the strength of the wooden laminations and the strength of the finger joints. Aligning these two factors is essential for enhancing the performance of GLT beams.

Colling [5] analyzed data from 38 studies covering fifteen wood species published between 1924 and 1988. The study concluded that GLT beams failing at finger joints exhibit a mean bending strength approximately 20% lower than those with wood failures in the laminations. Colling [5] further noted that the experiments mainly involved smaller beams without finger joints in high tensile stress areas, limiting the occurrence of potential finger-joint failures. In general, the number of finger joints in GLT beams varies considerably based on timber board length and defect removal for higher strength classes [4]. Consequently, efforts were made to enhance finger-joint strength to increase the bending strength of GLT beams.

In the 1990s, several studies (e.g., [5–8]) examined finger-joint failures in GLT beams. Notably, Falk et al. [6] tested 312 beams across three strength classes, comparing the characteristic bending strengths of beams that failed at finger joints with those that failed in the laminations. The study found that the strengths were comparable, with a maximum deviation of about 5%. This suggests similar statistical characteristics between the groups failing at finger joints and those failing within the laminations. In two strength classes, beams with finger-joint failures even exhibited higher characteristic bending strengths than those with failures in the laminations.

Aasheim and Solli [7] found that finger joints were not any weaker than natural defects, based on tests of beams with depths of 300 mm and 600 mm. In both cases, beams that failed at finger joints exhibited mean bending strengths comparable to the overall sample. For the larger beams, the mean strength of joint-failing specimens was about 3% lower than the overall mean, while for the smaller beams, it was about 6% higher. About one-quarter of the failures originated at the joints, corresponding to only six beams per size. The small number of observed failures limits the ability to identify a clear trend in the bending strength of joint-failing beams across the two sizes. Nevertheless, considering the similar mean strengths and assuming adequate quality control during manufacturing, the influence on the 5th-percentile bending strength of the entire sample appears to be limited. Similarly, Schickhofer [8] reported that finger joints did not represent the primary weak points and noted the increasing difficulty in determining failure causes as beam size increases due to the larger stressed volume in the tension zone.

The occurrence of finger-joint failures across varying beam sizes and two softwood strength classes was studied by Fink et al. [13] using numerical simulations. Their findings indicated that finger-joint failures become less frequent as beam size increases. This trend is attributed to the smaller variation in the strength of finger joints compared to weak sections in timber under tensile loading. The coefficient of variation for finger joints under tensile loading is about 0.2 [37], much lower than the coefficient for timber, which is 0.3 according to [38]. Consequently, weak sections within the timber are more likely to occur than finger-joint weaknesses as beam size increases. Additionally, the higher of the two strength classes in [13] (GL36h, according to EN 1194:1999 [39]) showed a greater frequency of finger-joint failures. However, this shortcoming was mitigated in EN 14080:2013 [32], which replaced EN 1194:1999 [39], by adjusting the required finger-joint strengths for individual strength classes and eliminating the highest strength class (GL36h).

The frequency of wood failures leading to collapse in exemplary experimental studies [6,10,12] ranges from 58% to 83%, underscoring the importance of understanding wood failure mechanisms. These studies focused on softwoods, while the driving failure mechanisms have been reported to differ for hardwoods [40]. To focus on the failure mechanisms in softwood, Kandler et al. [11] derived effective properties for tested GLT beams with well-known knot morphology and no finger joints. These effective properties, presented in property profiles (Fig. 1), provided the basis for the present work. Proper manufacturing and quality control of finger joints enable the efficient production of GLT beams whose strength is not compromised by the joints, thereby shifting the focus to the failure mechanisms of the wood itself.

The present modeling approach addresses failure mechanisms within the timber without incorporating finger joints. Although finger joints are undeniably a critical component of GLT, their performance has improved over the past decades, with current standards [32] being stricter than before. Based on the provided reasoning, only a limited effect on the statistical characteristics of large sample sizes is expected. Nevertheless, the main focus of this work is independent of finger-joint failure. This study primarily examines the influence of different global failure criteria and analyzes the progressive damage states of the implemented failure mechanisms within the modeling approach presented in the following section.

2.4. Modeling approach

The approach models GLT beam sections subjected to a constant bending moment (Fig. 2) and captured the entire load–displacement paths, including the load drop. Detailed descriptions of the method are provided in [15,26]. The simulations were conducted using a nonlinear finite element method within the software Abaqus [41]. The boards were assembled into GLT beam sections with homogeneous layups of strength classes GL24h and GL30h, following EN 14080:2013 [32], through a pseudo-random process. The final beam section consisted of continuous timber boards without finger joints. Each board featured section-wise constant properties, representing clear wood as well as defects such as knots and knot clusters. The load was applied in a displacement-controlled manner at an extended length e to minimize load-application effects. The model accounted for two progressive failure mechanisms: discrete cracking and plastic deformations.

Crack patterns in GLT are typically complex, so their effective implementation in the approach involved simplifying the crack directions to purely vertical and horizontal. Vertical cracks, occurring within individual boards, were modeled using XFEM, while horizontal cracks,

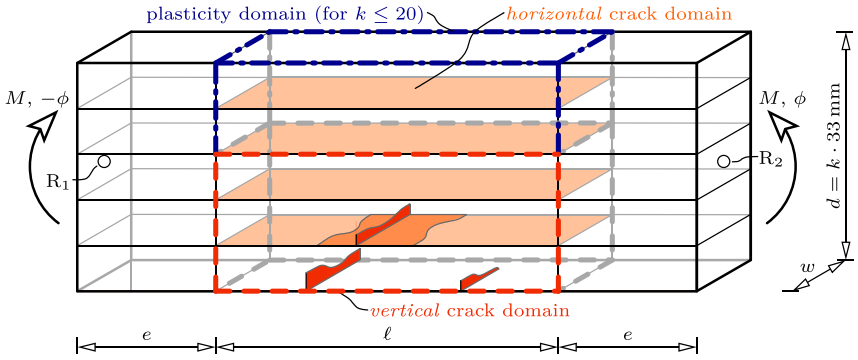

Fig. 2. Representative GLT beam section of length ℓ, depth d, and width w assembled by k laminations. The rotation ϕ generating the bending moment M was imposed at the extended length e.
Source: Adapted from [15].

occurring between boards, were realized by simulating the failure of cohesive surfaces. These horizontal cracks facilitated the interaction of vertical cracks but did not represent glue line failure. To improve numerical stability, a viscous regularization scheme was applied to the discrete cracking implementation. On the compression side of the beam sections, plastic deformation was incorporated for beam depths up to 660 mm.

Cracking was initiated when the stress exceeded a certain threshold, and the subsequent failure progression followed a linear traction–separation law governed by a specified fracture energy. Vertical cracks could occur in the bottom half of the beam, with initiation based on the tensile strength profile of the boards, ranging from 10 N/mm^2 to 55 N/mm^2. The upper limit aligns with the modeling results reported by Lukacevic et al. [42], which are on the lower end compared to other experimental results in the literature. Horizontal cracks could develop between all boards, using a tensile strength of 5 N/mm^2 perpendicular to the grain and a shear strength of 6 N/mm^2, consistent with experimental and modeling data in [42,43]. However, the tensile strength perpendicular to the grain is relatively high compared to other values reported in the literature.

The fracture energies were constant for both crack directions: 30 N/mm for vertical cracks and 0.6 N/mm for horizontal cracks. These values are in line with those reported in the literature. For instance, Jockwer [44] reports mode 1 fracture energy perpendicular to the grain $G_{\mathrm{f,h,I}}$ as 0.3 N/mm and mode 2 as 1.15 N/mm, based on multiple studies compiled in his work. In mixed-mode failures, the fracture energy falls between these values, depending on the dominance of each failure mode [45]. For vertical cracks, the fracture energy in mode 1 parallel to the grain $G_{\mathrm{f,v,I}}$ is about two orders of magnitude higher than in mode 1 perpendicular to it [46], resulting in a fracture energy of approximately 30 N/mm ($G_{\mathrm{f,v,I}} \approx 100 \cdot G_{\mathrm{f,h,I}}$).

The plastic deformations were modeled using ideal plasticity in conjunction with a multisurface failure criterion [42,47]. This criterion incorporates eight failure surfaces derived from the Tsai–Wu failure criterion [48]. The implementation was realized by employing a robust return mapping algorithm, as proposed by Pech et al. [49].

To increase computational efficiency, the approach exploited symmetry by modeling only half the beam width and using mesh refinement. Two element layers were used over the board depth and three layers over half the beam width w in regions where vertical cracking could occur. The element length was approximately equal to the element depth. For the remaining boards, a single element layer was applied across both the depth and width, with an element length of approximately 60 mm. The analysis used eight-node hexahedron elements with tri-linear shape functions. The adequacy of this mesh size is demonstrated in [15], where the approach is also validated against experimental data.

2.5. Simulation campaign

The simulation campaign in [15] covered seven beam depths ranging from 165 mm to 3300 mm (Fig. 3). The included size range extends well beyond those covered by experimental studies, as further discussed in Section 4.4, but it reflects the ongoing trend toward larger structural elements in building practice. The simulated beam sections were designed with a length-to-depth (ℓ/d) ratio of 1.5 to investigate the effects of both beam length and depth within the same set of simulations. This approach was particularly beneficial because the time required for nonlinear calculations increases substantially with beam size.

The simulated beams were assigned to strength classes GL24h and GL30h, as defined by EN 14080:2013 [32], and assembled from boards of strength classes T14 and T22, respectively, as introduced in Section 2.2. The properties of these boards were deterministically derived [19], in contrast to the stochastic approaches used by Fink et al. [13] and Frese and Blaß [14]. Capturing the variability of properties along the boards is essential in modeling. For example, Kandler et al. [50] showed that including MOE variation within boards significantly affects the simulated beam stiffness compared to assigning each board a constant MOE. Similarly, Soriano et al. [51] demonstrated experimentally that steel reinforcement can mitigate stiffness differences observed between beams.

This study employed a total of 11 800 simulations with $\ell/d = 1.5$ from the previous study in [15]. The number of simulations varied depending on the GLT beam section size (Table 1). As beam size increased, fewer simulations were required to capture the variability of material properties, with convergence determined by the 5th-percentile bending strength. For beam depths ranging from 165 mm to 660 mm, simulations were conducted with and without considering plastic deformations. This work uses the simulations considering plasticity unless otherwise specified. Identical beam layouts and material properties enabled a direct comparison of the influence of plastic deformations on individual beams.

2.6. Global failure criteria

The global failure criterion establishes the simulated load-bearing capacity M_{f}. Models in the literature have applied different global failure criteria, leading to differing size effects for large GLT beams [13–15]. These criteria were related to the progressive failure state, system stiffness, or loading. The presented modeling approach captures the entire load–displacement path and progressive damage during loading, allowing for the application and comparison of such criteria within this framework.

This work addresses the application of three global failure criteria, based on their implementation in the literature. The applied definitions were as follows:

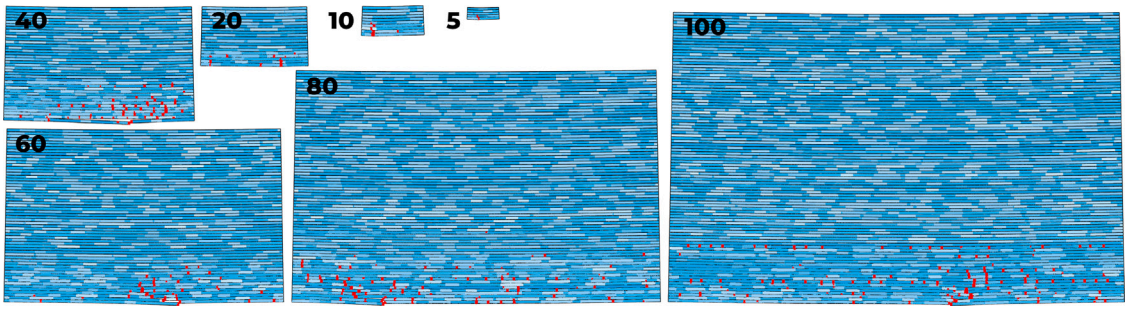

Fig. 3. Examples of the seven GLT beam section sizes, constructed with 5 to 100 laminations. The effective longitudinal modulus of elasticity E_L is shown in *blue*, with shading from light to dark representing increasing values. Vertical cracks are highlighted in *red*. [15]. (For interpretation of the references to color in this figure legend, the reader is referred to the web version of this article.)

Table 1
Simulated beam depths with the corresponding number of laminations and sample size for each strength class.

Depth d (mm)	Laminations k (–)	Sample size n (–)
165	5	1600[a]
330	10	400[a]
660	20	400[a]
1320	40	400
1980	60	300
2640	80	200
3300	100	200

[a] Individually for simulations considering or disregarding plastic deformations.

- The *load-drop* criterion (LoadC-3%) determined M_f when the load dropped by 3% relative to the maximum bending moment reached so far. This criterion was used in [15,26].
- The *stiffness-reduction* criterion (StiffnessC-1%) was fulfilled when the system stiffness reduced by 1% relative to the initial system stiffness at the first loading increment. This criterion was applied in a study by Fink et al. [13].
- The *crack-initiation* criterion (CrackC) identified M_f based on the initiation of the first vertical crack in the outermost tensile lamination. Frese and Blaß [14] used a similar criterion, evaluating failure within a lamination at a different vertical position using only a single element over its cross-section, in contrast to the present approach with a finer discretization.

When any of these criteria were met, the maximum bending moment M_{max} achieved up to that point was recorded as M_f. To ensure that the influence of the applied stabilization remained negligible throughout the entire loading path up to reaching the capacity M_f, the energy criterion

$$c_f = \frac{E_{ALLVD} + E_{ALLCD}}{E_{ALLIE} - E_{ALLCD}} \leq 5\% \tag{1}$$

was evaluated. The energy terms follow the notation used in Abaqus [41]. The criterion compares the energies dissipated through viscous regularization of vertical cracking E_{ALLVD} and horizontal cracking E_{ALLCD} to the total strain energy E_{ALLIE}. Because E_{ALLCD} is already included in E_{ALLIE}, it is subtracted from the denominator to prevent overestimation due to double counting. Subsequently, M_f was used to calculate the MOE E_{GLT} and bending strength f_b of the beam sections according to beam theory.

The calculation of E_{GLT} followed the method outlined by EN 408:2010+A1:2012 [52], using two specific loading points, M_1 and M_2, at 10% and 40% of M_f, along with their corresponding rotations, ϕ_1 and ϕ_2,

$$E_{GLT} = \frac{12\,(\ell + 2\,e)}{w d^3} \cdot \frac{M_2 - M_1}{2\,(\phi_2 - \phi_1)}, \tag{2}$$

where the dimensions ℓ, e, w and d are according to Fig. 2. The calculation of f_b assumed a linear stress distribution across the cross-section

$$f_b = \frac{6\,M_f}{w d^2}. \tag{3}$$

3. Simulated load–displacement paths

The modeling approach provided the load–displacement path for each simulation, with the bending moment M as the load and the rotation ϕ as the displacement. The simulated paths revealed three distinct types of structural behavior: approximately linear (Fig. 4a), pronounced pre-peak nonlinearities (Fig. 4b), and those containing horizontal plateaus (Fig. 4c). These behavior types have also been observed in experiments, e.g., reported in [3,9–11].

The results further demonstrated that the applied global failure criteria can lead to varying simulated load-bearing capacities, even when the load–displacement path appears approximately linear. Three scenarios highlight this variation, where the maximum load-bearing capacity in the simulation was marked by a striking load drop. In the first scenario, all three criteria yield nearly the same load-bearing capacity (Fig. 4d). In the second scenario, the first crack in the outermost tensile lamination occurs before the system stiffness decreases by 1% (Fig. 4e). Conversely, in the third scenario, the stiffness reduction precedes the crack initiation in the outermost tensile lamination (Fig. 4f).

Typically, a load drop marks global failure in experiments, making it a robust criterion. To assess the sufficiency of the applied 3% load-drop criterion, the results were compared with those obtained using 1% and 5% load drops. Identical results were found in 91% and 99% of the simulations, respectively. Therefore, the 3% load drop was sufficient for identifying the load-bearing capacity as the maximum load in a simulation.

In 50% and 67% of the simulations, the stiffness-reduction and crack-initiation criteria, respectively, yielded results deviating more than 10% from those obtained with the load-drop criterion. This variation underscores the considerable influence of the selected global failure criteria. Generally, the load-drop criterion yielded the highest load-bearing capacity, with only 0.11% (16 out of 7000) of the simulations identifying a higher capacity using the crack-initiation criterion.

With the load-drop criterion identifying the maximum capacity, the other two criteria highlight their specific characteristics during loading: the point of stiffness reduction and the first vertical crack initiation in the outermost tensile lamination. The simulated load-bearing capacities M_f from the stiffness-reduction and crack-initiation criteria,

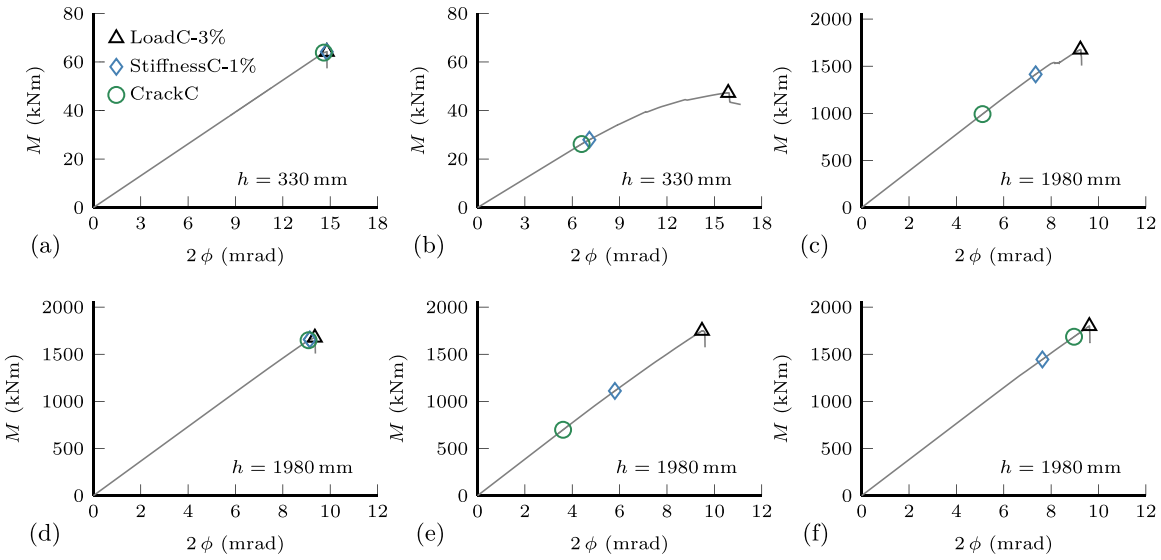

Fig. 4. Examples of load–displacement (M–ϕ) paths, showing (a–c) the three types of structural behavior and (d–f) exemplary sequences in which the criteria were met.

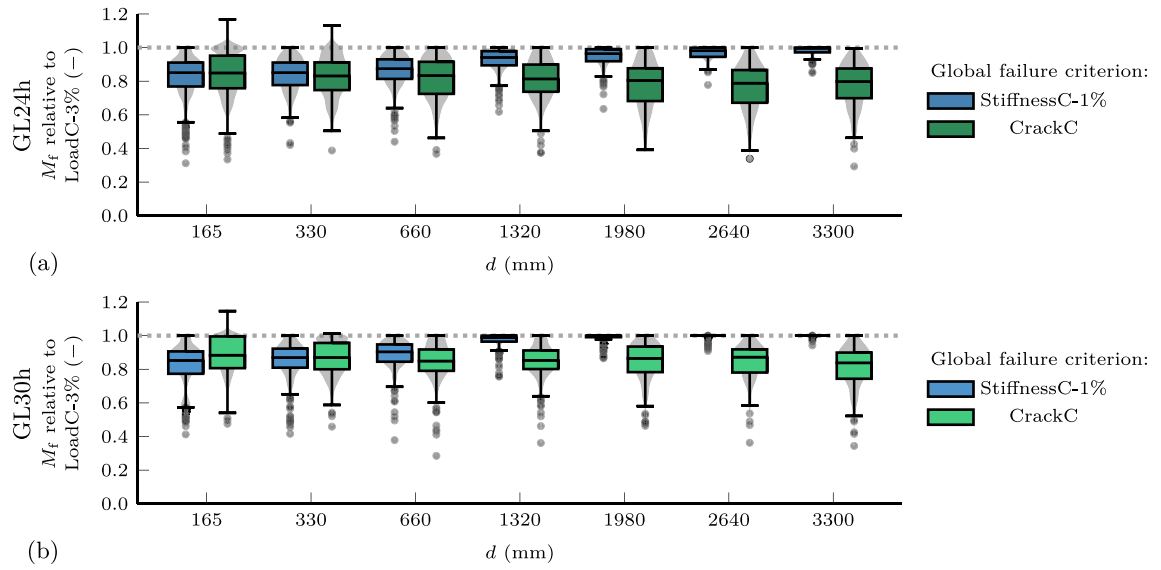

Fig. 5. Boxplots of simulated load-bearing capacities M_f obtained by the stiffness-reduction and crack-initiation criteria relative to the load-drop criterion for strength classes (a) GL24h and (b) GL30h across varying beam depths d. The boxplot edges represent the 25th and 75th percentiles, with the median marked by the middle line and whiskers extending up to 1.5 times the interquartile range.

relative to the load-drop criterion, showed distinct trends (Fig. 5). For the stiffness-reduction criterion, divergence decreased with increasing beam size, indicating a more linear load–displacement response during loading. The crack-initiation criterion maintained a consistent median with relatively large scatter across varying beam depths, suggesting that the first vertical crack in the outermost tensile lamination typically initiates at about 84% of maximum capacity, regardless of size.

Out of all 11 800 simulations, only two exceeded the energy criterion in Eq. (1) by 2.7% and 0.2% when employing the crack-initiation and load-drop criteria, respectively, in different simulations. For 0.3% of the simulations (36 in total), the load-bearing capacity failed to be determined using the same criterion. In these cases, no vertical crack was observed in the outermost tensile lamination, even though the load had already dropped by at least 10%. Therefore, the load-bearing capacity was taken as the maximum load observed throughout the entire simulation.

4. Analysis of material properties

4.1. Purpose and scope

The simulated load–displacement paths served as the basis for calculating the MOE E_{GLT} and bending strength f_b for the three applied global failure criteria. These results enable the comparison of each criterion's influence on E_{GLT} (Sections Section 4.2) and f_b (Sections Section 4.3). Assessing the changes in the 5th-percentile (characteristic) bending strength $f_{b,k}$ across different beam sizes reveals the size effect, which highlights the varying trends observed for each criterion (Section 4.4).

The primary focus of this section is on comparing the results between the applied global failure criteria; nonetheless, it is also of interest to compare the simulated effective properties with those from

other studies and the values provided in EN 14080:2013 [32]. The standard [32] specifies the material properties for GLT beams with a reference depth of $d_{\mathrm{ref}} = 600\,\mathrm{mm}$. The experimental setup for determining the effective properties of GLT beams follows EN 408:2010+A1:2012 [52], where a constant bending moment is applied to a span six times the depth ($\ell/d = 6.0$). While the ℓ/d ratio influences f_{b}, E_{GLT} remains unaffected, as demonstrated, e.g., in [15].

Consequently, E_{GLT} was directly obtained from simulations with a ratio of $\ell/d = 1.5$, as was f_{b} using the stiffness-reduction criterion. By contrast, f_{b} determined by the crack-initiation and load-drop criteria required adaptation to account for the correct ℓ/d ratio. In those cases, the procedure outlined in [15] was applied to adjust the n simulation results with $\ell/d = 1.5$ for the ratio 6.0:

$$f_{\mathrm{b},i} = \min\left(f_{\mathrm{b},(i-1)\cdot 4+1},\, f_{\mathrm{b},(i-1)\cdot 4+2},\, f_{\mathrm{b},(i-1)\cdot 4+3},\, f_{\mathrm{b},(i-1)\cdot 4+4}\right), \tag{4}$$

where $i \in \{1, \ldots, \lfloor n/4 \rfloor\}$ and $\lfloor\cdot\rfloor$ denotes the floor function that rounds $\cdot$ to the nearest smaller integer.

4.2. Modulus of elasticity

The simulated E_{GLT} was nearly identical across the three applied global failure criteria. In 99.9% of the simulations, the results from the crack-initiation and stiffness-reduction criteria deviated by less than 1% from those obtained using the load-drop criterion. The largest deviation observed among all simulations was 5.1%.

As reported for the load-drop criterion in [15], the comparison of the mean E_{GLT} values for both strength classes with those provided in EN 14080:2013 [32] revealed a maximum deviation of about 7%. Given the model assumptions, e.g., deriving the boards' individual stiffness tensors through a micromechanical multiscale model and adjusting them based on the geometric reconstruction of each board, these deviations are considered acceptable and relatively small.

4.3. Bending strength

The simulated f_{b} was strongly affected by the three applied global failure criteria, resulting in different trends for varying beam depths d (Fig. 6). For the results of each beam depth, a two-parameter log-normal probability distribution function (PDF) was fitted using maximum likelihood estimation. A log-normal distribution is used to estimate the 5th-percentile bending strength of GLT beams, as specified by EN 14358:2016 [53], and it is also recommended by JCSS [38] for probabilistic modeling. The mean and characteristic strength values, $f_{\mathrm{b,mean}}$ and $f_{\mathrm{b,k}}$, were taken from the PDFs. The results of both strength classes, obtained using the same criterion, exhibited generally similar characteristics.

When using the load-drop criterion (Fig. 6a,b), the mean values decreased as beam depth increased. Notably, larger beams with depths of at least 1320 mm exhibited much lower variation compared to smaller beams. The stiffness-reduction criterion similarly showed a decrease in mean values with increasing beam depth, but the characteristic values remained relatively stable due to reduced variation (Fig. 6c,d). In contrast, the crack-initiation criterion resulted in a decrease in both mean and characteristic values as beam size increased (Fig. 6e,f). In this case, the strength levels were generally lower and the variation across all beam sizes was mostly consistent.

4.4. Size effect on the characteristic bending strength

The three different global failure criteria resulted in varying trends for $f_{\mathrm{b,k}}$ across different beam sizes. These differences are emphasized by evaluating the size effect, which was obtained using the framework provided in prEN 1995-1-1:2023 [54]. In this approach, the characteristic reference bending strength $f_{\mathrm{b,k,ref}}$ for beams with a reference depth $d_{\mathrm{ref}} = 600\,\mathrm{mm}$, as specified by EN 14080:2013 [32], is adjusted by the depth modification factor $k_{\mathrm{h}}(d)$, which depends on the beam depth d in millimeters:

$$f_{\mathrm{b,k}}(d) = f_{\mathrm{b,k,ref}} \cdot k_{\mathrm{h}}(d) \quad \text{with} \quad k_{\mathrm{h}}(d) = \left(\frac{600}{d}\right)^{1/m}, \tag{5}$$

where m is a power-law parameter set to $m = 12.5$. In prEN 1995-1-1:2023 [54], this adjustment is limited to $k_{\mathrm{h}} \leq 1.1$. To determine the size effect in this work, $f_{\mathrm{b,k,ref}}$ and m were identified through least squares fitting of the simulation results for each applied criterion individually (Table 2).

Table 2
Fitted characteristic reference bending strength $f_{\mathrm{b,k,ref}}$ and power-law parameter m for the two strength classes GL24h and GL30h using the three global failure criteria.

Criteria	GL24h		GL30h	
	$f_{\mathrm{b,k,ref}}$ ($\mathrm{N/mm^2}$)	m (−)	$f_{\mathrm{b,k,ref}}$ ($\mathrm{N/mm^2}$)	m (−)
LoadC-3%	25.74	13.50	31.23	12.69
StiffnessC-1%	22.73	−171.94	28.44	−117.81
CrackC	15.61	6.77	20.85	7.13

The observed size effect varied considerably depending on the applied global failure criterion (Fig. 7). The trend is influenced by m, where smaller positive values lead to a greater decrease in strength for larger beam sizes, and a negative m indicates the opposite effect. The $f_{\mathrm{b,k,ref}}$ values identified from the load-drop and stiffness-reduction criteria align with those specified in EN 14080:2013 [32]. The strength classes GL24h and GL30h correspond to $f_{\mathrm{b,k,ref}}$ values of $24\,\mathrm{N/mm^2}$ and $30\,\mathrm{N/mm^2}$, respectively. The maximum deviation of $f_{\mathrm{b,k,ref}}$ from these classes was less than 8%, demonstrating reasonable agreement. Considering the model assumptions, e.g., related to the strength profiles and the constant fracture energies, these deviations are acceptable and relatively small. In contrast, the crack-initiation criterion significantly underestimated the strength values, with deviations of up to 35%.

At first glance, this pronounced underestimation may seem surprising, since the approach from which the crack-initiation criterion was adapted [14] produced bending strengths consistent with the standard, as shown, e.g., by Frese [55]. However, the differing results in this study can be explained by variations in the modeling strategy compared to that of Frese and Blaß [14]. Appendix A discusses the two main factors responsible for these discrepancies.

The load-drop criterion exhibited a size effect that was intermediate between the other two criteria. The stiffness-reduction criterion resulted in a nearly constant $f_{\mathrm{b,k}}$ across different beam sizes, consistent with the findings of Fink et al. [13], where the same criterion was applied to simulated beams with depths ranging from 320 mm to 1200 mm. In contrast, the crack-initiation criterion showed a more pronounced decrease in $f_{\mathrm{b,k}}$ with increasing beam size. A similar decrease was observed by Frese and Blaß [14], based on the progressive failure of the outermost tensile lamination, in simulations covering beam depths from 300 mm to 3000 mm.

Experimental data for GLT beams of varying sizes, tested according to the setup specified in EN 408:2010+A1:2012 [52] and based on lamination grading compliant with European standards, are scarce. Aasheim and Solli [7] and Schickhofer [8] conducted such tests on beams with depths of 300 mm and 600 mm. Their results provide characteristic bending strengths based on fitted PDFs, enabling estimation of the power-law parameter m for different strength classes (Table 3) and thus allowing comparison with the simulation results.

The experimental data align well with the trend predicted by the simulations using the load-drop criterion (Fig. 7). While the tested beams included finger joints, the modeling approach did not explicitly represent them (as discussed in Section 2.3). Moreover, as experimental data with sufficiently large sample sizes are only available for beams up to 600 mm, extrapolation to larger depths introduces uncertainty.

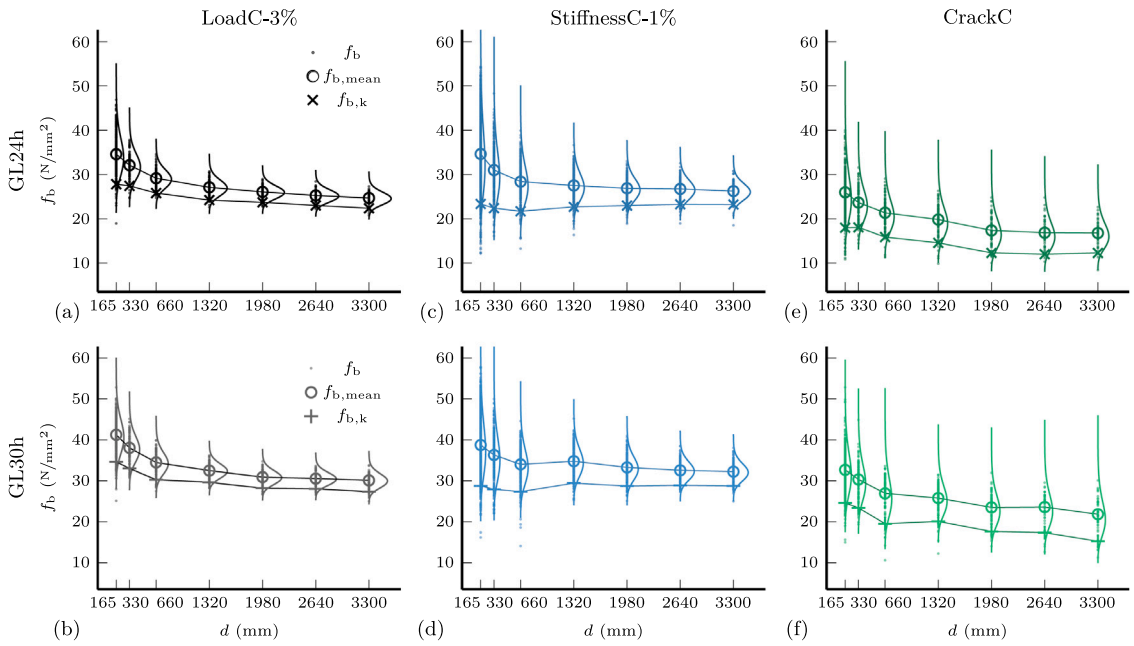

Fig. 6. Simulated bending strength f_b with marked mean $f_{b,mean}$ and 5th percentile (characteristic) $f_{b,k}$ based on fitted log-normal PDFs for beams with depth d and strength classes GL24h or GL30h, obtained using (a,b) the load-drop criterion, (c,d) the stiffness-reduction criterion, and (e,f) the crack-initiation criterion.

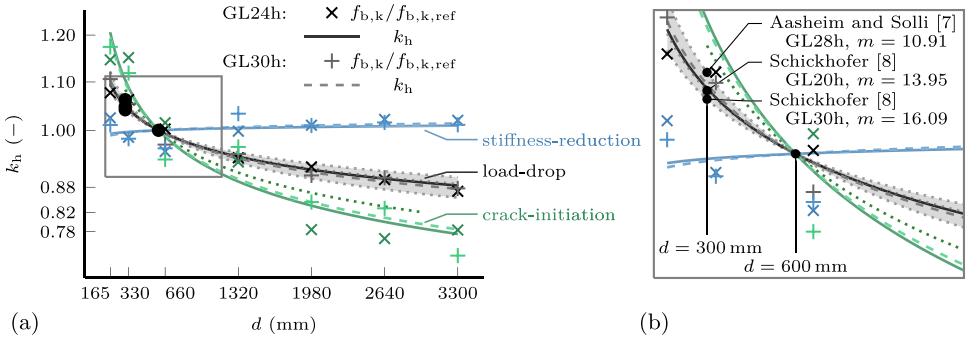

Fig. 7. Depth modification factor k_h across varying depths d corresponding to the three global failure criteria: load-drop, stiffness-reduction, and crack-initiation. The *dotted green* line represents the depth modification proposed by Frese and Blaß [14]. *Black dots* represent experimental results (Table 3), with the *gray shading* indicating their extrapolated range. (a) Full depth range from 165 mm to 3300 mm, (b) zoomed view of the smaller beam depths highlighting the experimental results.

Table 3
Characteristic reference bending strength $f_{b,k,ref}$ and power-law parameter m from experimental data for variable strength classes.

Study	Strength class		Applied PDF	Parameters	
	Reported[a]	Mapped[b]		$f_{b,k,ref}$ (N/mm²)	m (−)
Aasheim and Solli [7]	T30	GL28h	3-parameter Weibull	32.0	10.91
Schickhofer [8]	MS10h	GL20h	lognormal	21.6	13.95
Schickhofer [8]	MS17h	GL30h	lognormal	31.8	16.09

[a] Reported in the corresponding study.
[b] Mapped according to EN 14080:2013 [32].

5. Analysis of the progressive damage states

5.1. Purpose and scope

The presented modeling approach incorporated multiple progressive failure mechanisms that accumulate until the simulated beam section collapsed. The progression of damage during loading indicates how much stress redistribution the structure can accommodate. The ultimate failure was effectively detected by the load-drop criterion. This approach offers a valuable opportunity to closely examine the implemented failure mechanisms, i.e., cracks that simulate quasi-brittle failure and plastic deformations in regions under compressive stresses. Of particular interest is the spreading depth of damage due to cracks at failure and its correlation with bending strength across various beam depths. The insights gained here contribute to the understanding of the implemented failure mechanisms and support the development of future models.

Data in the literature on experimentally observed or simulated wooden failure mechanisms of GLT during loading is limited. Experimental data is often restricted to visible cracks on the exterior surface observed during loading, which indicate substantial damage to the wooden structure, while the actual failure likely initiates much earlier

at a smaller scale. Progressive damage states of simulated GLT beams are rarely reported in the literature, e.g., only exemplary results are presented in [55,56].

This section analyzes the progression of vertical and horizontal cracking (Section 5.2) and effects of plastic deformations (Section 5.3) across all seven simulated beam depths. The three applied criteria refer to specific points during the loading, providing insights into the progression of damage within the model. Estimating the spread of modeled damage relative to beam depth across varying sizes, prior to any calculations, is challenging due to the highly nonlinear effects of discrete cracking implementations and the increasing model length with beam depth.

5.2. Vertical and horizontal cracking

The modeled cracks were implemented using traction–separation laws to simulate quasi-brittle material failure. Crack initiation marked the beginning of the damage process, during which the opposing crack surfaces continued to transfer stresses. As the separation of the crack surfaces increased, the transferred tensile and shear stresses progressively decreased. Once the modeled damage has fully developed, the crack completely separated the surfaces, allowing for their independent movement. Consequently, the modeled cracks represent the full spectrum of damage from initiation to completion, whereas experimentally visible cracks typically indicate substantial damage.

To quantify the simulated damage caused by cracking, the number of damaged laminations $k_{\mathrm{d}}^{\mathrm{v}}$ and the number of damaged interfaces between adjacent laminations $k_{\mathrm{d}}^{\mathrm{h}}$ were used. A lamination or interface was considered damaged if a vertical or horizontal crack was initiated. Each beam consisted of k laminations and $k-1$ interfaces. The damage was evaluated at the load-bearing capacities determined by the three global failure criteria. The application of the three criteria provided a comprehensive overview of the damage states corresponding to their specific characteristics.

The following analysis first focuses on the damage state at ultimate failure, identified by the load-drop criterion, to provide an overview of the frequency and progression of cracking (Section 5.2.1). Subsequently, two damage assessment methods are compared to highlight the non-consecutive spread of damage (Section 5.2.2). This is followed by a discussion of damage trends across the simulated beam sizes, revealing the relation between damage and beam depth (Section 5.2.3). Finally, the correlation between bending strength and the extent of damage is examined to assess whether observed damage can be considered an indicator of strength (Section 5.2.4).

The online supplementary material includes figures for each beam depth, showing the probability of damage in at least a given number of laminations and interfaces, along with their correlation to bending strength (see Appendix B for link).

5.2.1. Damage at ultimate failure

Most laminations exhibited damage across their entire cross-section at ultimate failure, but the overall progression of this damage remained moderate. In contrast, damage to the interfaces was concentrated in relatively small areas compared to the total interface area. The details of this analysis are:

- Out of the total number of simulated laminations with possible vertical cracks, 30% (26 367 out of 88 400 laminations) showed damage. Among the damaged laminations, 72% had damage spanning the entire cross-section. Each cross-section comprised six elements, and the evolution of damage in an individual element could range from 0% to 100%. When considering the mean value of all elements within a cross-section, 99% of the damaged laminations had a mean damage evolution smaller than 45% for the most severely damaged cross-section within each lamination.
- Regarding all interfaces, 19% (32 484 out of 173 000 interfaces) exhibited damage. Of the damaged interfaces, 81% had damage spread over an area smaller than 5% of the interface area $A_{\mathrm{int}} = \ell \cdot w$. Four nodes were positioned across the interface width, taking advantage of symmetry, where each node could represent the damage evolution within the range of 0% to 100%. Among the damaged interfaces, 58% had a maximum mean damage evolution greater than 80% for the four nodes across the width.

5.2.2. Damage quantification methods

Two methods were employed to further quantify damage: First, damage in *consecutive* order, which tracks the number of consecutively damaged laminations starting from the outermost tensile side and progressing through the beam depth, regardless of when the crack occurred. Second, the *non-consecutive* damage, which corresponds to the total number of damaged laminations without considering their position within the beam. These methods were also applied to evaluate the damaged interfaces.

The number of consecutively and non-consecutively damaged laminations and interfaces increased with greater beam depth d. The discontinuous spread of damage over d is reflected in the difference between these two evaluation methods, as demonstrated by the simulations with $d = 660\,\mathrm{mm}$ in Fig. 8. The figure presents the empirical complementary cumulative distribution function (CCDF) $P(X \geq x)$, representing the probability of damage occurring in at least a given number of laminations or interfaces. The three applied failure criteria capture different damage states during loading. The load-drop criterion generally showed a higher probability of damage than the other two, evidenced by the vertical offset of the markers, highlighting the potential for further damage accumulation up to the point of load drop.

5.2.3. Trends across beam sizes

The extent of damage was evaluated by analyzing relative damage across all simulated beam sizes. Relative damage is defined as the number of damaged laminations relative to the total number of laminations, $k_{\mathrm{d}}^{\mathrm{v}}/k$, and analogously for interfaces, $k_{\mathrm{d}}^{\mathrm{h}}/(k-1)$. The comparison is based on non-consecutive damage counts and specific values at $P = 50\%$ and $P = 90\%$ of the empirical CCDF, where P represents the probability of observing at least the corresponding relative damage (Fig. 8).

The load-drop criterion showed relatively consistent relative damage for beams with $d \geq 1320\,\mathrm{mm}$ (Fig. 9), suggesting that the damage-affected region scales proportionally with beam size. For the larger beams, the stiffness-reduction criterion generally yielded relative damage comparable to those from the load-drop criterion, indicating brittle failure behavior in their load–displacement paths. The crack-initiation criterion consistently resulted in the lowest relative damage. The observed high relative damage in smaller beams were caused by their lower number of laminations k and interfaces $k-1$. Comparing the two strength classes, the lower strength class exhibited higher relative damage than the higher one.

5.2.4. Correlation with bending strength

The relationship between bending strength f_{b} and damage of laminations and interfaces was evaluated at ultimate failure. For beams with depths $d \geq 1980\,\mathrm{mm}$ ($k \geq 60$), the Pearson correlation coefficient ρ exceeded 0.42 and increased with beam size, reaching up to $\rho = 0.76$. A stronger correlation indicates that a higher f_{b} tend to coincide with a greater extent of damage. Since damage initiation triggers stress redistribution, this suggests that stress redistribution contributes to the homogenization of f_{b}, as reflected in the reduced strength variability for larger beams. Such a reduction has been reported in simulation studies [15,57] and is further supported by experimental data [58].

However, the lowest f_{b} within each size and strength class (14 simulation sets) corresponded to the simulations with the lowest number of damaged laminations or interfaces in only four and two sets, respectively, based on the load-drop criterion. Therefore, the lowest f_{b} was only occasionally associated with the least damage, indicating that fewer numbers of damaged laminations or interfaces cannot be used as a reliable indicator of low bending strength.

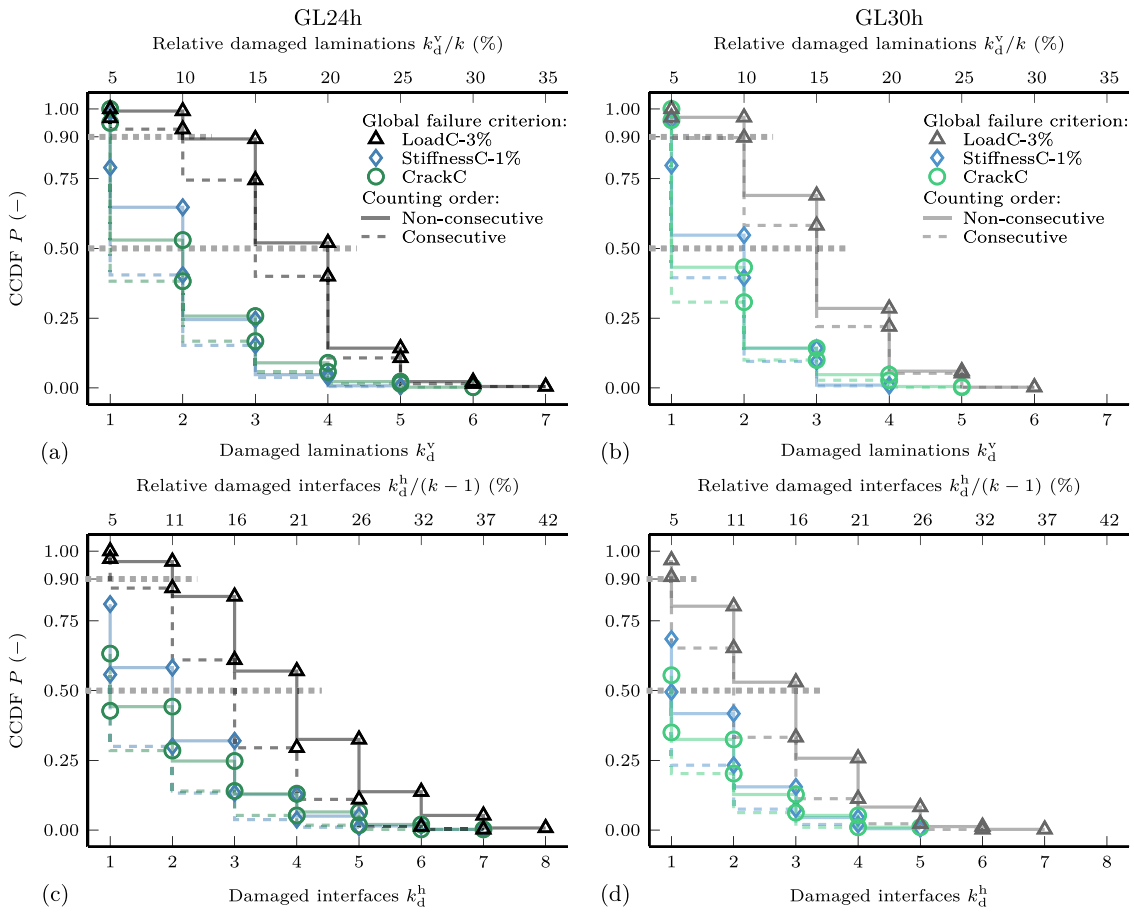

Fig. 8. Probability P of observing at least k_d damaged laminations or interfaces. Results are shown for (a, b) laminations k_d^v and (c, d) interfaces k_d^h, across three global failure criteria, strength classes (a, c) GL24h and (b, d) GL30h, at beam depth $d = 660$ mm with $k = 20$ laminations. Horizontal gray dashed lines at 50% and 90% mark the proportion of simulations that meet or exceed the corresponding damage.

5.3. Plastic deformation

Plastic deformations were modeled using a multisurface failure criterion [42,47,49]. To evaluate their impact on the bending strength f_b, each beam layout was simulated twice, considering either elastic or elastic–plastic behavior on the compressive side. Experimental studies indicate that plastic deformations are more pronounced in smaller beams and higher strength classes [11,13], so the comparison focused on beam depths up to 660 mm. The bending strengths $f_{b,el}$ and $f_{b,pl}$ were determined, and their ratio $f_{b,el}/f_{b,pl}$ highlights the influence of the applied global failure criteria.

Considering all three criteria, plasticity had only a negligible influence on bending strength (±2%) for two-thirds of the simulated beams at a depth of 660 mm (Fig. 10). When evaluated using the load-drop criterion, 88% of the simulations showed a variation within ±2%. However, a few individual beams exhibited a greater response, with plasticity influencing results by up to 5%. The crack-initiation criterion showed even less influence overall and at the individual beam level. In contrast, the stiffness-reduction criterion revealed a significant influence on a significant proportion of the sample, particularly for the higher strength class. This influence reflects the nonlinear shape of the load–displacement paths. A generally minor impact of plastic deformations on f_b was also reported by Frese [55] for beams subjected to four-point bending tests according to EN 408:2010+A1:2012 [52] with $d = 600$ mm.

The plasticity effects were stronger among simulations of the smaller beam sizes (Fig. 11). For beams with a depth of 165 mm, only about half (54%) of the simulations using the load-drop criterion showed a negligible influence (±2%). More simulations fell within this range when applying the stiffness-reduction (65%) and crack-initiation (81%) criteria. However, the stiffness-reduction criterion also revealed substantial outliers: in 10% of the simulations, $f_{b,el}$ was at least 30% higher than $f_{b,pl}$ for the lower strength class and 67% higher for the higher strength.

Generally, plastic deformations reduced the observed strength $f_{b,pl}$ because, according to beam theory, plastic compression on one side of the cross-section leads to an increase in linear distributed tensile stresses on the opposite side. The Pearson correlation coefficient ρ between $f_{b,pl}$ and $f_{b,el}/f_{b,pl}$ was weak, reaching a maximum of 0.52 for 660 mm deep beams of strength class GL30h. Higher strength classes experienced a greater impact, consistent with plastic deformations occurring primarily under high compressive stresses.

Figures detailing effects of plastic deformations, along with their correlation to bending strength, are available for each beam depth in the online supplementary material (see Appendix B for link).

6. Conclusion and outlook

Based on an extensive numerical simulation campaign consisting of 11 800 simulations, various global failure criteria definitions were employed to investigate their influence on the MOE, bending strength, and implemented failure mechanisms. The failure mechanisms in the modeling approach of GLT beams included vertical cracking within the laminations, horizontal cracking between them, and plastic deformations in the zone subjected to compressive loads. The study encompassed beam sizes with depths ranging from 165 mm to 3300 mm and analyzed the implemented progressive failure mechanisms in detail.

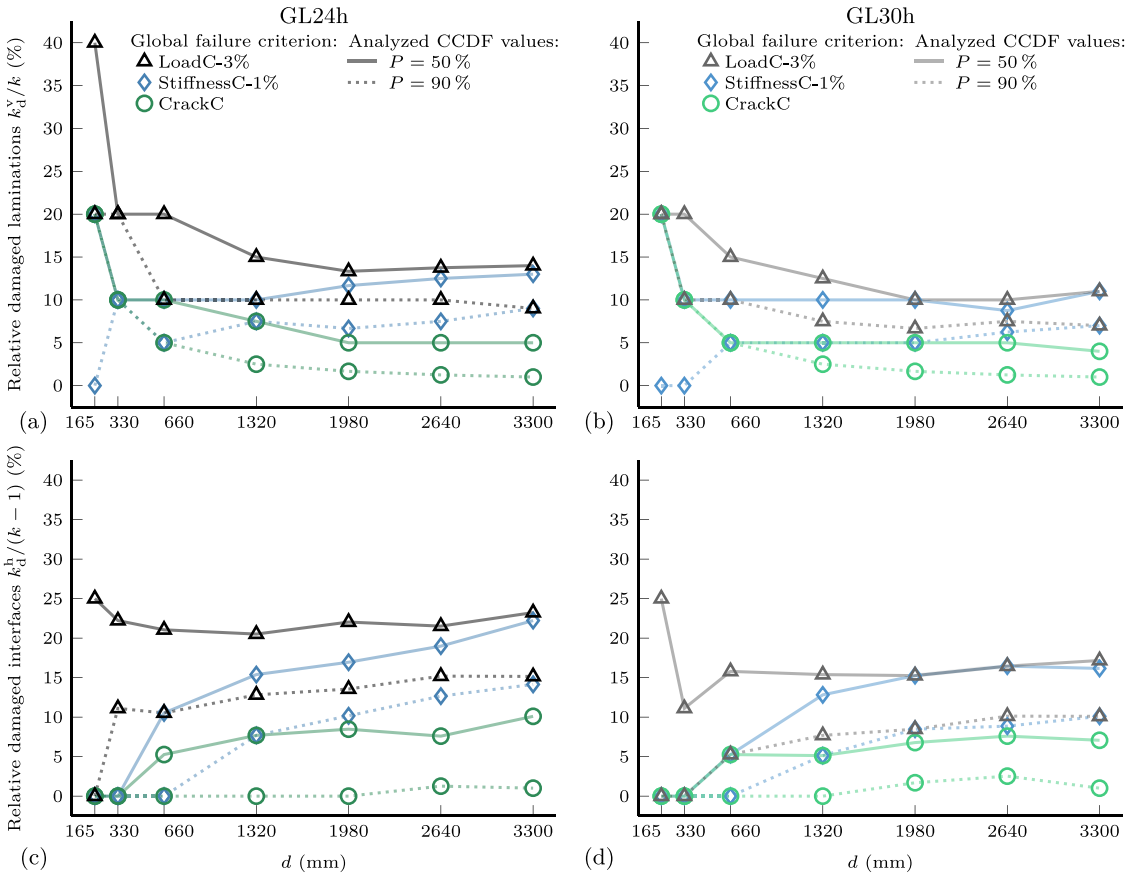

Fig. 9. Relative damaged (a, b) laminations $k_{\mathrm{d}}^{\mathrm{v}}/k$ and (c, d) interfaces $k_{\mathrm{d}}^{\mathrm{h}}/(k-1)$ across varying beam depths d. Results are shown for the three global failure criteria at two empirical CCDF probabilities, representing the proportion of simulations with at least the respective relative damage, and for strength classes (a, c) GL24h and (b, d) GL30h. Damage counts were recorded in a non-consecutive order.

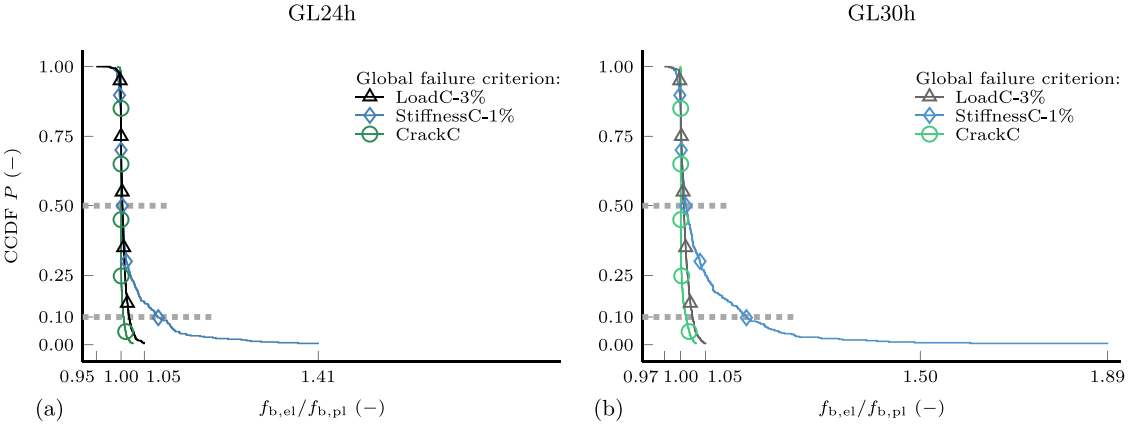

Fig. 10. Probability P of observing at least the strength ratio $f_{\mathrm{b,el}}/f_{\mathrm{b,pl}}$. Results are shown for the three global failure criteria, a beam depth $d = 660\,\mathrm{mm}$ with $k = 20$ laminations, and strength classes (a) GL24h and (b) GL30h. Horizontal gray dashed lines at 10% and 50% mark the proportion of simulations that meet or exceed the corresponding strength ratio.

From our in-depth analysis of the simulation results, the following conclusions are drawn:

- The choice of the global failure criterion significantly influences the predicted bending strength, while the MOE remains practically unaffected. In the presented modeling approach, the 3% load-drop criterion effectively captured the maximum simulated load. The stiffness-reduction criterion provided insight into the nonlinearity of the load–displacement paths, which became more linear with increasing beam size. The crack-initiation criterion identified the onset of the first crack in the outermost tensile lamination, showing considerable variability across all sizes in relation to the eventual load-bearing capacity.
- The differing size-effect trends emphasize the importance of the selected global failure criterion. The trends for the stiffness-reduction and crack-initiation criteria align with those reported in the literature, where these criteria were originally applied using different modeling strategies. For large beams, the crack-initiation criterion resulted in a greater strength decrease than observed by

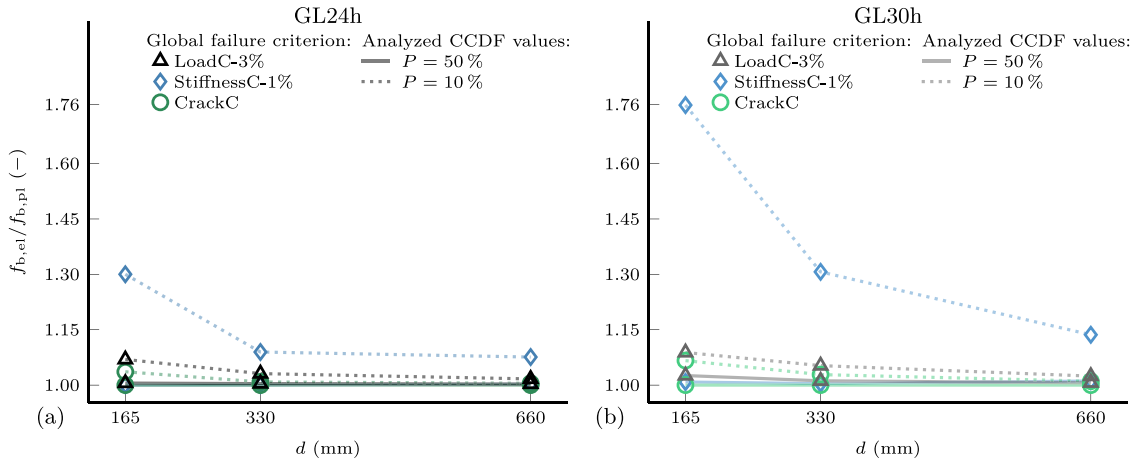

Fig. 11. Strength ratio $f_{b,el}/f_{b,pl}$ across varying beam depths d. Results are shown for the three global failure criteria at two empirical CCDF probabilities, representing the proportion of simulations with at least the respective strength ratio, and for strength classes (a) GL24h and (b) GL30h.

the load-drop criterion, whereas the stiffness-reduction criterion showed no sensitivity to beam size.

- The loading process triggers progressive failure mechanisms that accumulate until ultimate failure, indicated by a load drop. During this process, substantial stress redistribution can occur. Among the evaluated criteria, the load-drop and the crack-initiation criteria generally showed the highest and lowest damage levels, respectively.
- The damage at load-bearing capacity, relative to the number of laminations k, remained constant for beams with $d \geq 1320\,\text{mm}$ when evaluated using the load-drop criterion. This consistency suggests that the damage-affected zone expands proportionally with the increasing number of laminations, spreading across the beam depth during loading. The relative damage identified by the crack-initiation criterion follows a similar trend to the load-drop criterion but consistently yields lower values. In contrast, the relative damage based on the stiffness-reduction criterion gradually approaches that of the load-drop criterion as beam size increases.
- The effect of plastic deformations on the bending strength is limited in large sample sizes, as shown by simulations using the load-drop and crack-initiation criteria. However, individual beams, especially smaller ones and those in the higher strength class, were substantially impacted by plastic deformations, resulting in a lower bending strength. An even more pronounced strength reduction in a significant proportion of samples was observed when using the stiffness-reduction criterion, highlighting its sensitivity to early nonlinearity in the load–displacement response.

For future work, the constant fracture energies should be refined to section-wise constant values. These individual fracture energies can be determined through detailed numerical simulations of knot sections using the phase-field method for fracture simulation, a promising approach demonstrated by Pech et al. [59,60]. These simulations are expected to also improve the accuracy of strength profiles. Additionally, the integration of finger joints would enable valuable assessments of their influence on the structural behavior of GLT beams.

Numerical simulation approaches, such as the one used in this study, offer a wide range of applications. They enable the generation of extensive datasets that can support data-driven methods. For example, Pech et al. [61] applied metaheuristic algorithms to minimize the deflection of GLT beams assembled from predefined board sets. Such datasets can also serve as a basis for statistical mechanics-based methods [62], which may enable the development of more tailored and efficient timber design strategies. When focused on failure processes, simulations can provide deeper insight into damage mechanisms, improving structural assessments and informing decisions on criticality and retrofitting.

CRediT authorship contribution statement

Christoffer Vida: Conceptualization, Methodology, Software, Validation, Formal analysis, Investigation, Writing – original draft, Visualization. **Markus Lukacevic:** Conceptualization, Methodology, Writing – review & editing. **Georg Hochreiner:** Conceptualization, Methodology, Writing – review & editing. **Sebastian Pech:** Conceptualization, Methodology, Writing – review & editing. **Josef Füssl:** Conceptualization, Methodology, Writing – review & editing, Supervision, Funding acquisition.

Declaration of competing interest

The authors declare that they have no known competing financial interests or personal relationships that could have appeared to influence the work reported in this paper.

Acknowledgments

This research was funded in whole or in part by the Austrian Science Fund (FWF) [Y1093–N30] and [F77]. For open access purposes, the author has applied a CC BY public copyright license to any author accepted manuscript version arising from this submission. The authors acknowledge TU Wien Bibliothek for financial support through its Open Access Funding Program.

Appendix A. Main factors behind deviating results using the crack-initiation criterion

Two main factors are responsible for the lower bending strengths observed when applying the crack-initiation criterion, compared to the studies by Frese and Blaß [14] and Frese [55], from which the criterion was adapted: (i) the input tensile strength and (ii) the discretization of the laminations in the tensile zone.

(i) The simulated tensile strengths of laminations used as input in [55] can be significantly higher than corresponding experimental results, depending on the strength class, as shown in ([55], Fig. 2-10). For the strength classes GL24h and GL30h, as defined by EN 14080:2013 [32], the corresponding sets of strength-graded laminations are listed in ([55], Table 3-2). The simulated characteristic tensile strengths of these sets, reported in ([55], Figs. 7-2 and 7-3), exceed the standard values associated with the respective strength classes T14

and T22 (used for GL24h and GL30h) by 6.2 N/mm^2 and 6.7 N/mm^2, respectively.

(ii) Frese and Blaß [14] and Frese [55] employed a discretization with one element across the lamination thickness, resulting in stress evaluation at mid-depth. In contrast, the present approach uses a finer discretization with two elements, shifting the stress evaluation to the quarter-point. This leads to a different vertical position at which the failure criterion evaluates stress. The influence of this positional shift can be expressed by the geometric factor

$$k_a = 1 + \frac{t}{2(d-t)}, \tag{A.1}$$

where t is the lamination thickness and d is the beam depth. For the reference beam size with d = 600, mm and t = 33, mm, the factor becomes

$$k_a = 1 + \frac{33}{2(600-33)} = 1.029. \tag{A.2}$$

These two main factors have a significant impact on the simulated bending strength of the beams. The difference in characteristic tensile strength between the input and the standard values can be interpreted as a shift in the entire strength distribution, with higher tensile strength directly leading to increased bending strength. Additionally, the geometric factor k_a accounts for the difference in the vertical position at which stress is evaluated.

By applying the respective tensile strength differences to the results from the crack-initiation criterion (Table 2) and multiplying by the geometric factor k_a, adjusted characteristic bending strengths $f^*_{b,k,ref}$ can be calculated to correct for the identified deviations:

$$\text{GL24h:} \quad f^*_{b,k,ref} = (15.6 + 6.2) \cdot 1.029 = 22.4\,\text{N/mm}^2, \tag{A.3}$$

$$\text{GL30h:} \quad f^*_{b,k,ref} = (20.9 + 6.7) \cdot 1.029 = 28.4\,\text{N/mm}^2. \tag{A.4}$$

These adjusted values align well with the characteristic bending strengths obtained using the load-drop and stiffness-reduction criteria (Table 2), and are in reasonable agreement with the values specified for GL24h and GL30h in EN 14080:2013 [32].

Appendix B. Damage results per beam depth

Supplementary material related to this article can be found online at https://doi.org/10.1016/j.engstruct.2025.121489.

Data availability

Data will be made available on request.

References

[1] Moe J. Strength and stiffness of glued laminated timber beams. No. 5, Norsk Skogindustri; 1961.

[2] Larsen HJ. Strength of glued laminated beams. Report 8201, Aalborg University; 1982.

[3] Ehlbeck J, Colling F, Görlacher R. Einflußkeilgezinkter Lamellen auf die Biegefestigkeit von Brettschichtholzträgern. Report, Universität Karlsruhe; 1984.

[4] Ehlbeck J, Colling F. Biegefestigkeit von Brettschichtholz in Abhängigkeit von Rohdichte, Elastizitätsmodul, Ästigkeit und Keilzinkung der Lamellen, der Lage der Keilzinkung sowie von der Trägerhöhe. Teil A: Karlsruher Untersuchung. Report, Universität Karlsruhe; 1987.

[5] Colling F. Tragfähigkeit von Biegeträgern aus Brettschichtholz in Abhängigkeit von den Festigkeitsrelevanten Einflussgrößen (Ph.D. thesis), Karlsruhe, Germany: Universität Karlsruhe; 1990.

[6] Falk RH, Solli KH, Aasheim E. The performance of glued laminated beams manufactured from machine stress graded norwegian spruce. Meddelelse 77, Norsk Treteknisk Institutt; 1992.

[7] Aasheim E, Solli KH. Size factor of Norwegian glued laminated beams. In: Proc. 28th CIB-W18 Meet., CIB-W18/28-12-2. Copenhagen, Denmark; 1995.

[8] Schickhofer G. Development of efficient glued laminated timber. In: Proc. 29th CIB-W18 Meet., CIB-W18/29-12-1. Bordeaux, France; 1996.

[9] Blaß HJ, Schmid M. Optimierung der Bemessung von Brettschichtholz mit maschinell sortierten Lamellen. Report, Universität Karlsruhe; 2005.

[10] Fink G, Frangi A, Kohler J. Bending tests on GLT beams having well-known local material properties. Mater Struct 2015;48:3571–84. http://dx.doi.org/10.1617/s11527-014-0424-2.

[11] Kandler G, Lukacevic M, Füssl J. Experimental study on glued laminated timber beams with well-known knot morphology. Eur J Wood Wood Prod 2018;76:1435–52. http://dx.doi.org/10.1007/s00107-018-1328-6.

[12] Fink G, Stadelmann P, Frangi A. Bending test on large-scale GLT beams with well-known beam setup using machine grading indicator. Int Wood Prod J 2021;12:258–66. http://dx.doi.org/10.1080/20426445.2021.1969166.

[13] Fink G, Frangi A, Kohler J. Probabilistic approach for modelling the load-bearing capacity of glued laminated timber. Eng Struct 2015;100:751–62. http://dx.doi.org/10.1016/j.engstruct.2015.06.015.

[14] Frese M, Blaß HJ. Numerical description of size and load configuration effects in glulam structures. In: Proc. 12th Int. Conf. Appl. Stat. Probab. Civ. Eng., ICASP12. Vancouver, Canada; 2015, http://dx.doi.org/10.14288/1.0076135.

[15] Vida C, Lukacevic M, Hochreiner G, Füssl J. Size effect on bending strength of glued laminated timber predicted by a numerical simulation concept including discrete cracking. Mater Des 2023;225:111550. http://dx.doi.org/10.1016/j.matdes.2022.111550.

[16] Ehlbeck J, Colling F, Görlacher R. Einflußkeilgezinkter Lamellen auf die Biegefestigkeit von Brettschichtholzträgern: Eingangsdaten für das Rechenmodell. Holz als Roh- Werkst 1985;43:369–73. http://dx.doi.org/10.1007/BF02607906.

[17] Görlacher R. Klassifizierung von Brettschichtholzlamellen durch Messung von Longitudinalschwingungen (Ph.D. thesis), Karlsruhe, Germany: Universität Karlsruhe; 1990.

[18] Fink G, Kohler J. Model for the prediction of the tensile strength and tensile stiffness of knot clusters within structural timber. Eur J Wood Wood Prod 2014;72:331–41. http://dx.doi.org/10.1007/s00107-014-0781-0.

[19] Kandler G, Lukacevic M, Zechmeister C, Wolff S, Füssl J. Stochastic engineering framework for timber structural elements and its application to glued laminated timber beams. Constr Build Mater 2018;190:573–92. http://dx.doi.org/10.1016/j.conbuildmat.2018.09.129.

[20] Lam F. Size effect of bending strength in glulam beams. In: Proc. 44th CIB-W18 Meet., CIB-W18/44-12-5. Alghero, Italy; 2011.

[21] Ehlbeck J, Colling F, Görlacher R. Einflußkeilgezinkter Lamellen auf die Biegefestigkeit von Brettschichtholzträgern: Entwicklung eines Rechenmodells. Holz als Roh- Werkst 1985;43:333–7. http://dx.doi.org/10.1007/BF02607817.

[22] Ehlbeck J, Colling F, Görlacher R. Einflußkeilgezinkter Lamellen auf die Biegefestigkeit von Brettschichtholzträgern: Überprüfung des Rechenmodells mit Hilfe von Trägerversuchen. Holz als Roh- Werkst 1985;43:439–42. http://dx.doi.org/10.1007/BF02612470.

[23] Bažant ZP, Chen E-P. Scaling of structural failure. Appl Mech Rev 1997;50:593–627. http://dx.doi.org/10.1115/1.3101672.

[24] Blank L, Fink G, Jockwer R, Frangi A. Quasi-brittle fracture and size effect of glued laminated timber beams. Eur J Wood Wood Prod 2017;75:667–81. http://dx.doi.org/10.1007/s00107-017-1156-0.

[25] Tapia Camú C, Aicher S. A stochastic finite element model for glulam beams of hardwoods. In: Proc. 11th World Conf. Timber Eng., WCTE 2018. Seoul, Republic of Korea; 2018.

[26] Vida C, Lukacevic M, Eberhardsteiner J, Füssl J. Modeling approach to estimate the bending strength and failure mechanisms of glued laminated timber beams. Eng Struct 2022;255:113862. http://dx.doi.org/10.1016/j.engstruct.2022.113862.

[27] Lamy F, Takarli M, Angellier N, Dubois F, Pop O. Acoustic emission technique for fracture analysis in wood materials. Int J Fract 2015;192:57–70. http://dx.doi.org/10.1007/s10704-014-9985-x.

[28] Landis EN, Belalpour Destjerdi P. Acoustic emissions in wood. In: Grosse CU, Ohtsu M, Aggelis DG, Shiotani T, editors. Acoustic Emission Testing: Basics for Research – Applications in Engineering. Cham, Switzerland: Springer International Publishing; 2022, p. 567–82. http://dx.doi.org/10.1007/978-3-030-67936-1_19.

[29] Aicher S, Dill-Langer G. Fracture location by NDT in glulam loaded in tension perpendicular to the grain. In: 11th International Symposium on Nondestructive Testing of Wood. Madison, Wisconsin, USA; 1998.

[30] Ni P, Li J, Hao H, Yan W, Du X, Zhou H. Reliability analysis and design optimization of nonlinear structures. Reliab Eng Syst Saf 2020;198:106860. http://dx.doi.org/10.1016/j.ress.2020.106860.

[31] Goswami S, Yin M, Yu Y, Karniadakis GE. A physics-informed variational DeepONet for predicting crack path in quasi-brittle materials. Comput Methods Appl Mech Engrg 2022;391:114587. http://dx.doi.org/10.1016/j.cma.2022.114587.

[32] EN 14080:2013. Timber Structures – Glued Laminated Timber and Glued Solid Timber – Requirements. Standard, Brussels, Belgium: European Committee for Standardization; 2013.

[33] Kandler G, Lukacevic M, Füssl J. An algorithm for the geometric reconstruction of knots within timber boards based on fibre angle measurements. Constr Build Mater 2016;124:945–60. http://dx.doi.org/10.1016/j.conbuildmat.2016.08.001.

[34] EN 338:2016. Structural Timber – Strength Classes. Standard, Brussels, Belgium: European Committee for Standardization; 2016.

[35] Hofstetter K, Hellmich C, Eberhardsteiner J. Micromechanical modeling of solid-type and plate-type deformation patterns within softwood materials. a review and an improved approach. Holzforschung 2007;61:343–51. http://dx.doi.org/10.1515/HF.2007.058.
[36] Lukacevic M, Füssl J, Eberhardsteiner J. Discussion of common and new indicating properties for the strength grading of wooden boards. Wood Sci Technol 2015;49:551–76. http://dx.doi.org/10.1007/s00226-015-0712-1.
[37] Vafadar F, Collins S, Fink G. Experimental investigation of finger joints under tensile and bending loads. In: Proc. 13th World Conf. Timber Eng., WCTE 2023. Oslo, Norway; 2023, http://dx.doi.org/10.52202/069179-0091.
[38] JCSS. Probabilistic Model Code – Part 3: Resistance Models (3.05 Timber). 2006.
[39] EN 1194:1999. Timber Structures – Glued Laminated Timber – Strength Classes and Determination of Characteristic Values. Standard, Brussels, Belgium: European Committee for Standardization; 1999.
[40] Aicher S, Stapf G. Glulam from European white oak: finger joint influence on bending size effect. In: Aicher S, Reinhardt H-W, Garrecht H, editors. Materials and joints in timber structures. Volume 9 of *RILEM* bookseries, Dordrecht: Springer Netherlands; 2014, p. 641–56.
[41] Abaqus. Abaqus 2021 HF5, Software. Rhode Island, United States, Rhode Island, United States: Dassault Systèmes Simulia Corp.; 2021.
[42] Lukacevic M, Lederer W, Füssl J. A microstructure-based multisurface failure criterion for the description of brittle and ductile failure mechanisms of clear-wood. Eng Fract Mech 2017;176:83–99. http://dx.doi.org/10.1016/j.engfracmech.2017.02.020.
[43] Eberhardsteiner J. Mechanisches Verhalten von Fichtenholz. Vienna, Austria: Springer Vienna; 2002, http://dx.doi.org/10.1007/978-3-7091-6111-1.
[44] Jockwer R. Structural Behaviour of Glued Laminated Timber Beams with Unreinforced and Reinforced Notches (Ph.D. thesis), Zurich, Switzerland: ETH Zurich; 2014, http://dx.doi.org/10.3929/ethz-a-010171641.
[45] Serrano E. Rational modelling and design in timber engineering applications using fracture mechanics. In: Proc. 10th World Conf. Timber Eng., WCTE 2016. Vienna, Austria; 2016.
[46] Jeronimides G. The fracture of wood in relation to its structure. Leiden Bot Ser 1976;3:253–65.
[47] Lukacevic M, Füssl J, Lampert R. Failure mechanisms of clear wood identified at wood cell level by an approach based on the extended finite element method. Eng Fract Mech 2015;144:158–75. http://dx.doi.org/10.1016/j.engfracmech.2015.06.066.
[48] Tsai SW, Wu EM. A general theory of strength for anisotropic materials. J Compos Mater 1971;5:58–80. http://dx.doi.org/10.1177/002199837100500106.
[49] Pech S, Lukacevic M, Füssl J. A robust multisurface return-mapping algorithm and its implementation in Abaqus. Finite Elem Anal Des 2021;190:103531. http://dx.doi.org/10.1016/j.finel.2021.103531.
[50] Kandler G, Füssl J, Serrano E, Eberhardsteiner J. Effective stiffness prediction of GLT beams based on stiffness distributions of individual lamellas. Wood Sci Technol 2015;49:1101–21. http://dx.doi.org/10.1007/s00226-015-0745-5.
[51] Soriano J, Pellis BP, Mascia NT. Mechanical performance of glued-laminated timber beams symmetrically reinforced with steel bars. Compos Struct 2016;150:200–7. http://dx.doi.org/10.1016/j.compstruct.2016.05.016.
[52] EN 408:2010+A1:2012. Timber Structures – Structural Timber and Glued Laminated Timber – Determination of Some Physical and Mechanical Properties. Standard, Brussels, Belgium: European Committee for Standardization; 2012.
[53] EN 14358:2016. Timber Structures – Calculation and Verification of Characteristic Values. Standard, Brussels, Belgium: European Committee for Standardization; 2016.
[54] prEN 1995-1-1:2023. Eurocode 5 – Design of Timber Structures – Part 1-1: General Rules and Rules for Buildings. Standard, Brussels, Belgium: European Committee for Standardization; 2023.
[55] Frese M. Computergestützte Verfahren zur pragmatischen Beurteilung der Tragwiderstände von Brettschichtholz: Zusammenfassung exemplarischer Simulationsstudien (Habilitation), Karlsruhe, Germany: Karlsruher Institut für Technologie (KIT); 2016, http://dx.doi.org/10.5445/KSP/1000052710.
[56] Blaß HJ, Frese M, Glos P, Denzler J, Linsenmann P, Ranta-Maunus A. Zuverlässigkeit von Fichten-Brettschichtholz mit modifiziertem Aufbau. Report, Universität Karlsruhe; 2008, http://dx.doi.org/10.5445/KSP/1000008462.
[57] Frese M, Blaß HJ. Reliability of large glulam members Part 1: Data for the assessment of partial safety factors for the bending strength. In: Proc. 49th INTER Meet., INTER/49-17-1. Graz, Austria; 2016.
[58] Fink G, Brandner R, Palma P, Kohler J. Volume effects in glued laminated timber beams. In: Proc. 14th Int. Conf. Appl. Stat. Probab. Civ. Eng., ICASP14. Dublin, Ireland; 2023.
[59] Pech S, Lukacevic M, Füssl J. A hybrid multi-phase field model to describe cohesive failure in orthotropic materials, assessed by modeling failure mechanisms in wood. Eng Fract Mech 2022;271:108591. http://dx.doi.org/10.1016/j.engfracmech.2022.108591.
[60] Pech S, Lukacevic M, Füssl J. Validation of a hybrid multi-phase field model for fracture of wood. Eng Fract Mech 2022;275:108819. http://dx.doi.org/10.1016/j.engfracmech.2022.108819.
[61] Pech S, Kandler G, Lukacevic M, Füssl J. Metamodel assisted optimization of glued laminated timber beams by using metaheuristic algorithms. Eng Appl Artif Intell 2019;79:129–41. http://dx.doi.org/10.1016/j.engappai.2018.12.010.
[62] Vida C, Lukacevic M, Pech S, Füssl J. Strength distribution predictions of glued laminated timber beams: Influence of size, load configuration, and strength class described by the finite weakest-link theory. Constr Build Mater 2025;458:139514. http://dx.doi.org/10.1016/j.conbuildmat.2024.139514.